Submitted to the ApJ
Preprint typeset using LaTeX style emulateapj v. 12/16/11

EVIDENCE FOR A MASSIVE, EXTENDED CIRCUMGALACTIC MEDIUM AROUND THE ANDROMEDA GALAXY[1]

Nicolas Lehner[1], J. Christopher Howk[1], and Bart P. Wakker[2]

Submitted to the ApJ

ABSTRACT

We demonstrate the presence of an extended and massive circumgalactic medium (CGM) around Messier 31 using archival *HST* COS ultraviolet spectroscopy of 5 QSOs projected within the virial radius ($R_{\rm vir}$ = 300 kpc). We detect Si III absorption associated with the M31 CGM toward all the 5 sightlines, including the most distant at ρ = 245 and 294 kpc, C IV and Si IV in 4 sightlines, and singly-ionized species toward only the three targets with $\rho \leq 50$ kpc. Two targets at ρ = 26 and 294 kpc were observed by *FUSE* and show O VI M31 CGM absorption. The M31 CGM gas is therefore multiphase, mostly ionized, and becomes more highly ionized gas at larger ρ. The detection of C IV and O VI absorption at $26 \leq \rho < 300$ kpc strongly suggests an extended hot corona around M31. We estimate using Si II, Si III, and Si IV a CGM metal mass of 2.9×10^6 M$_\odot$ and gas mass of $4 \times 10^9\,(Z_\odot/Z)$ M$_\odot$ within $1/6R_{\rm vir}$, implying nearly as much metal and gas mass within $1/6R_{\rm vir}$ of the CGM of M31 as in the disk of M31. We estimate the total metal mass and baryon mass of the cool M31 CGM gas at $R_{\rm vir}$ to be $\sim$ 2–10 $\times 10^7$ M$_\odot$ and $\sim$ 3–10 $\times 10^{10}$ M$_\odot$, respectively. Compared with galaxies in the larger COS-Halos survey, the CGM of M31 appears to be quite typical for a L^* galaxy.

Keywords: galaxies: halos — galaxies: individual (M31) — intergalactic medium — Local Group — quasars: absorption lines

1. INTRODUCTION

It is critical to characterize the circumgalactic medium (CGM) of galaxies since the large-scale inflows and outflows within the CGM are key ingredients in shaping galaxies and driving their evolution (e.g., Kereš et al. 2005; Dekel & Birnboim 2006; Faucher-Giguère & Kereš 2011; Putman et al. 2012). Observations of the properties of the CGM are therefore critital to test theories of galaxy evolution. Thanks to high quality ultraviolet observations, it is indisputable that the CGM is a massive reservoir of metals and baryons (e.g., Wakker & Savage 2009; Prochaska et al. 2011; Tumlinson et al. 2011; Werk et al. 2013, 2014; Lehner et al. 2013; Stocke et al. 2013; Peeples et al. 2014). These observational studies provide, however, only average properties of galaxies with a broad range of properties, and therefore the CGM properties such as gas kinematics, metal mass distribution, and ionization states as a function of galaxy geometry and properties are not well constrained.

With several tens of QSO sightlines going through the Milky Way (MW) CGM (e.g., Savage et al. 2003; Sembach et al. 2003; Wakker et al. 2003; Fox et al. 2006; Shull et al. 2009; Lehner et al. 2012), the MW would appear a perfect candidate for a "zoom-in" experiment, i.e., in which we can study the CGM along different sightlines of a single galaxy. However, our understanding of the MW CGM has remained somewhat limited by our position within the MW disk. For example, the high-velocity clouds (HVCs) that cover the Galactic sky are thought to probe the extended MW CGM. Their distances are now largely determined (Ryans et al. 1997; Wakker 2001; Thom et al. 2006, 2008; Wakker et al. 2007, 2008; Lehner & Howk 2010; Smoker et al. 2011 for H I HVC complexes and Lehner & Howk 2011; Lehner et al. 2012 for the diffuse ionized HVCs), but this created another puzzle since they place most of the HVCs within 5–15 kpc of the sun, not at 100–300 kpc, the expected size of the MW CGM, and hence the HVCs only represent a comparatively very small mass (since $M \propto d^2$). Only the Magellanic Stream (e.g., Putman et al. 1998; Brüns et al. 2005; Nidever et al. 2008; Fox et al. 2014) is more distant, possibly extending to 80–200 kpc (Besla et al. 2012), providing some evidence for an extended corona around the MW (e.g., Stanimirović et al. 2002; Sembach et al. 2003; Fox et al. 2013).

The strongest evidence for extended highly ionized CGM around L^* star-forming galaxies comes from the COS-Halos survey (Tumlinson et al. 2013), which shows that typically star-forming L^* galaxies have O VI column densities $N_{\rm OVI} \gtrsim 10^{14.3}$ cm^{-2} while more passive L^* galaxies show weaker or no O VI absorption in their CGM (Tumlinson et al. 2011). The high O VI column density found by COS-Halos is another element that shows that the HVCs do not probe the extended MW CGM since $N_{\rm OVI}$ for the MW HVCs is on average a factor 5 times smaller (see the results in Sembach et al. 2003; Fox et al. 2006). Only if the entire MW thick disk and halo absorption is integrated, $N_{\rm OVI}$ in the MW would approach $10^{14.3}$ cm^{-2} (i.e., by combining the results of Savage et al. 2003 and Sembach et al. 2003). This would mean that most of the column density of the MW

[1] Based on observations made with the NASA/ESA Hubble Space Telescope, obtained at the Space Telescope Science Institute, which is operated by the Association of Universities for Research in Astronomy, Inc. under NASA contract No. NAS5-26555.
[2] Department of Physics, University of Notre Dame, 225 Nieuwland Science Hall, Notre Dame, IN 46556
[3] Supported by NASA/NSF, affiliated with the Department of Astronomy, University of Wisconsin, 475 N. Charter Street, Madison, WI 53706

CGM might be hidden in the low-velocity component (see Peek et al. 2009). However, it is also plausible that the MW CGM has properties that are different from $z \sim 0.5$ L^* galaxies.

Studies of the gas content of nearby galaxies offer major advantages over both the MW and higher redshift galaxies. Nearby galaxies span a large angular extent and can be studied over multiple lines-of-sight and offer a direct mapping between the stellar distribution and the gas content. This experiment has been conducted for the Large Magellanic Cloud (Howk et al. 2002; Lehner & Howk 2007; Lehner et al. 2009; Barger et al. 2014; K. Barger et al., in prep.), showing in particular the presence of large-scale outflows from a sub-L^* galaxy. However, the L^* galaxy that can be observed with the most detail is Andromeda (M31).

The stellar disk and halo of M31 have been subject to intense study (e.g., Brown et al. 2006; McConnachie et al. 2009; Gilbert et al. 2012; Dalcanton et al. 2012), with well-determined local and global properties, including its inclination (Walterbos & Kennicutt 1987), stellar and virial masses (Geehan et al. 2006; van der Marel et al. 2012), dust and ISM disk mass (Draine et al. 2014), and rotation curve (e.g., Chemin et al. 2009). These studies all imply that M31 is fairly typical of massive star-forming galaxies,which has undergone several major interactions with its satellites (e.g., Gordon et al. 2006; Putman et al. 2009), and possibly in a phase of transformation into a red galaxy (Mutch et al. 2011; Davidge et al. 2012). The specific star-formation rate of M31, sSFR$\equiv$ SFR/M$_\star$ $= (5 \pm 1) \times 10^{-12}$ yr^{-1} (using the stellar mass M$_\star$ and SFR from Geehan et al. 2006; Kang et al. 2009), places M31 just between the passively evolving and star forming galaxies in COS-Halos (Tumlinson et al. 2011). As we show in this paper, the value of $N_{\rm OVI}$ in the CGM of M31 and the sSFR of M31 are also consistent with M31 being in the green valley.

Parallel to this intensive observational effort, there is also a major theoretical effort to understand the two massive galaxies, the MW and M31, of the Local Group (LG) (Richter 2012; Garrison-Kimmel et al. 2014; Nuza et al. 2014). With this large amount of empirical results, M31 should become the benchmark for assessing the validity of the physics implementations in these simulations. However, this requires to have also knowledge of its CGM. Deep studies of H I 21-cm emission at the level of $\log N_{\rm HI} \geq 17$ have reported the detections of H I clouds mostly along the M31–M33 axis (Thilker et al. 2004; Braun & Thilker 2004; Lockman et al. 2012; Wolfe et al. 2013), but, as for the MW, this H I detection might only be the tip of the iceberg and H I alone does not provide information on the gas-phases, the metal content, and hence the total metal and baryon masses.

We searched the *HST* Cosmic Origins Spectrograph (COS) and *Far Ultraviolet Spectroscopic Explorer* (*FUSE*) archives at MAST to find high resolution UV spectra of QSOs probing the CGM of M31, identifying 5 QSOs with UV spectra having signal-to-noise (S/N) sufficient to search and model the weak metal-line absorption features from the diffuse CGM gas of M31. While a much larger sample of sightlines will be needed to achieve our ultimate goal — to produce a global map of the kinematics and surface densities of low and high ions in the CGM of M31 — these 5 sightlines provide already important insights on the diffuse ionized CGM gas and its metal and baryon masses. We therefore report the analysis of these 5 sightlines through the CGM of M31 at $26 \leq \rho < 300$ kpc in this paper. We adopt throughout a distance of 770 kpc and a virial radius of 300 kpc for M31 (e.g., Ribas et al. 2005; van der Marel et al. 2012).

Table 1
Data Sample Summary

Target	l (°)	b (°)	ρ (kpc)	PI	HST ID
RXJ0048.3+3941	122.28	−23.18	26	Rich	11632
HS0033+4300	120.03	−19.51	31	Rich	11632
HS0058+4213	124.91	−20.34	50	Rich	11632
3C66A	140.14	−16.77	245	Stocke	12612
MRK335	108.76	−41.41	294	Green	11524

2. SAMPLE AND DATA ANALYSIS

In the *HST* COS archive we identified 5 targets with useable high-resolution UV spectra. All these targets were observed with the COS G130M and G160M gratings ($R \approx 16,000$). The sample is summarized in Table 1 with the *HST* program identification number and the PI for each program. In Fig. 1, we show the distribution of the targets in our sample overplotted with the H I contours from Braun & Thilker (2004). There are 3 targets within an impact parameter $\rho = 50$ kpc that are close to or near the H I contours and 2 targets between 240 and 300 kpc. The three inner targets are also part of another paper that will consider in more details the relation (if any) between the gas and stellar halos of M31 (C. Danforth et al. 2014, in prep.). We also found *FUSE* ($R \approx 15,000$) archival spectra for MRK335 and RXJ0048.3+3941 with sufficient S/N to detect and analyse the O VI λ1031 and C III λ977 absorption. The O VI absorption is particularly important since it gives a direct point of comparison with COS-Halos.

Information on the design and performance of COS and *FUSE* can be found in Green et al. (2012) and Moos et al. (2000), respectively. Detailed information about the COS and *FUSE* data processing can be found in Fox et al. (2014) and Wakker et al. (2003). In short, the exposures were aligned in wavelength space by matching the centroids of all the absorption lines visible in individual spectra. The coadded spectrum was then shifted into the LSR velocity frame by matching the centroids of the Galactic H I 21-cm emission in that direction from the LAB survey (Kalberla et al. 2005) to the absorption of neutral and singly ionized species. We normalized the QSO continua with low order Legendre polynomials within about $\pm$1000 km s^{-1} from the absorption under consideration; typically polynomials with orders $m \leq 4$ were fitted. In Figs. A1 to A5 of the appendix, we show the resulting normalized profiles against the LSR velocity. We remove from the O VI λ1031 absorption the H_2 contamination following the method described in Wakker et al. (2003) using the updated H_2 models along the MRK335 and RXJ0048.3+3941 sightlines from Wakker (2006). Figs. A1 and A5 show the

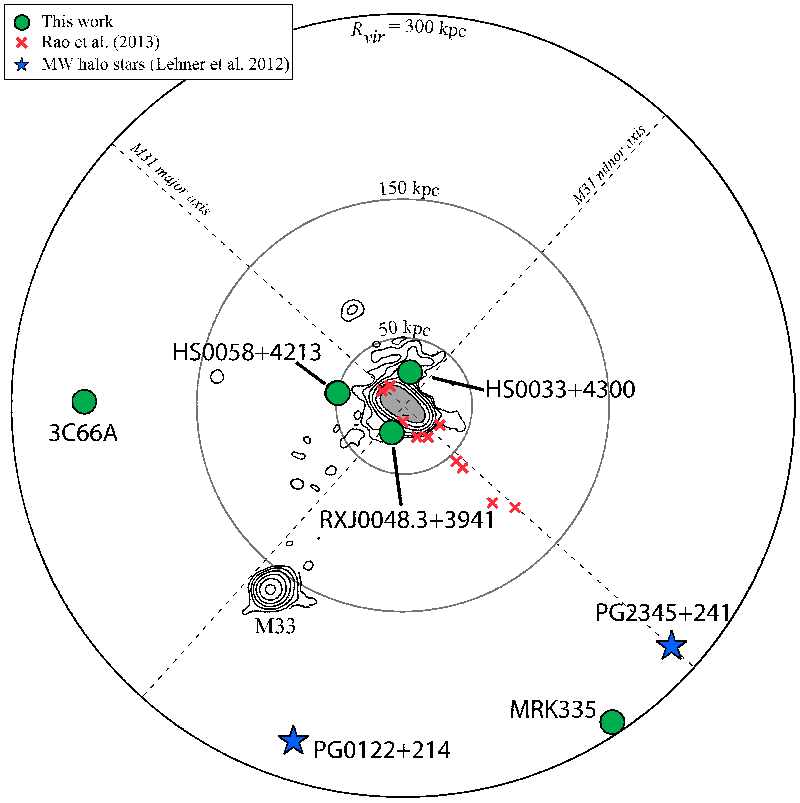

Figure 1. Distribution of the five targets in our sample in the CGM of M31 (right ascension increases from right to left, declination increases from bottom to top). All these these sightlines were observed with COS G130M and G160M and show ionized absorption at LSR velocities $-320 \lesssim v_{\rm LSR} \lesssim -150$ km s^{-1} associated with the CGM of M31. RXJ0048.3+3941 and MRK335 were also observed with *FUSE* and both have O VI absorption at similar LSR velocities. Overplotted is the H I 21-cm emission map around M31 adapted from Braun & Thilker (2004) where the lowest contour has $\log N_{\rm HI} = 17.5$ in the 40′ beam, with 0.5 dex increment between contours (this provides in our opinion a better representation of the H I distribution around M31 according to recent GBT observations, see Lockman et al. 2012; Wolfe et al. 2013). The crosses show for reference the targets from the COS G140L M31 program where only low ions (e.g., Mg II) were detected and only within the H I disk contour (i.e., $\rho \leq 32$ kpc, see Rao et al. 2013).

H_2 model, displaying that the 6–0 $P(3)$ H_2 line directly contaminates the O VI absorption in the velocity region of interest. However, based on previous experience, this contamination can be removed fairly accurately with an uncertainty of ±0.1 dex (Wakker et al. 2003).

To search for M31 CGM absorption and to determine the properties of the CGM gas, we consider the following atom and ions and transitions: O I λ1302, O VI λ1031, C II λ1334, C III λ977, C IV λλ1548, 1550, Si II λ1193 (because Si II λ1260 is blended with S II λ1259 near the systemic velocity of M31), Si III λ1206, and Si IV λλ1393, 1402. Other transitions are typically too weak to be detected and would not produce interesting limits.

We employed the apparent optical depth (AOD) method described by Savage & Sembach (1991) to estimate the total column density and average velocity of the metal ions. The absorption profiles are converted into apparent column densities per unit velocity, $N_a(v) = 3.768 \times 10^{14} \ln[F_c(v)/F_{\rm obs}(v)]/(f\lambda)$ cm^{-2} (km s^{-1})$^{-1}$, where $F_c(v)$ and $F_{\rm obs}(v)$ are the modeled continuum and observed fluxes as a function of velocity, respectively, f is the oscillator strength of the transition and λ is the wavelength in Å. The atomic parameters are for the UV transitions from Morton (2003). When no detection was observed, we estimated a 3σ upper limit following the method described by Lehner et al. (2008). The total column density was obtained by integrating over the absorption profile $N = \int_{v_1}^{v_2} N_a(v)dv$ and the average velocity was determined from the first moment $\langle v \rangle = \int_{v_1}^{v_2} vN_a(v)dv / \int_{v_1}^{v_2} N_a(v)dv$.

We integrate over the velocities associated with the M31 CGM gas, as explained in §3. In Table 2, we summarize the integration range for each sightline and the velocity and column density results for each species. We note a good agreement between the column densities measured for the doublet transitions (C IV, Si IV), showing no indication of saturation. We note, however, that C II and Si III for the 3 targets at $\rho \leq 50$ kpc could be somewhat saturated owing the peak apparent optical depth being $\tau_a \gtrsim 1$. In this table, we also list the average velocity (defined as $\langle v_{\rm all} \rangle$) based on all the reliable transitions for a given sightline.

Table 2
Kinematics and Column Densities

Species	(v_1, v_2) (km s^{-1})	$\langle v \rangle$ (km s^{-1})	$\log N$ [cm^{-2}]
RXJ0048.3+3941, $\rho = 26$ kpc, $\langle v_{\rm all} \rangle = -213.1 \pm 8.7$ km s^{-1}			
O I λ1302	−306, −150	···	< 13.63
C II λ1334	−306, −150	−188.7 :	14.57 :
Si II λ1193	−306, −150	-197.4 ± 2.0	13.43 ± 0.02
C III λ 977	−306, −150	−220.7 :	> 14.08
Si III λ1206	−306, −150	-215.5 ± 0.8	13.42 ± 0.01

Table 2 — *Continued*

Species	(v_1, v_2) (km s^{-1})	$\langle v \rangle$ (km s^{-1})	log N [cm^{-2}]
Si IV λ1393	−306, −150	-212.9 ± 1.3	13.38 ± 0.01
Si IV λ1402	−306, −150	-211.3 ± 2.6	13.41 ± 0.03
C IV λ1548	−306, −150	-218.8 ± 1.1	14.08 ± 0.02
C IV λ1550	−306, −150	-222.7 ± 2.0	14.11 ± 0.02
O VI λ1031	−306, −130	-209.4 ± 5.0	14.33 ± 0.10
HS0033+4300, $\rho = 31$ kpc, $\langle v_{\rm all} \rangle = -204.1 \pm 2.0$ km s^{-1}			
O I λ1302	−280, −150	···	< 14.26
C II λ1334	−280, −150	-204.1 ± 5.9	14.34 :
Si II λ1193	−280, −150	−223.8 :	13.36 ± 0.18
Si III λ1206	−280, −150	-201.2 ± 6.4	13.31 ± 0.10
Si IV λ1402	−280, −150	-206.8 ± 6.7	13.26 ± 0.09
C IV λ1548	−280, −150	-203.6 ± 3.0	14.04 ± 0.05
C IV λ1550	−280, −150	-204.6 ± 5.5	14.07 ± 0.08
HS0058+4213, $\rho = 50$ kpc, $\langle v_{\rm all} \rangle = -211.1 \pm 3.9$ km s^{-1}			
O I λ1302	−280, −150	···	< 14.02
C II λ1334	−280, −150	-214.1 ± 2.9	14.41 ± 0.06
Si II λ1193	−280, −150	-217.3 ± 5.9	13.45 ± 0.08
Si III λ1206	−280, −150	-210.5 ± 3.2	13.44 ± 0.08
Si IV λ1393	−280, −150	-207.4 ± 5.1	13.42 ± 0.07
Si IV λ1402	−280, −150	-212.4 ± 8.7	13.43 ± 0.12
C IV λ1548	−280, −150	-210.5 ± 4.3	13.95 ± 0.06
C IV λ1550	−280, −150	-205.8 ± 7.6	14.00 ± 0.10
3C66A, $\rho = 245$ kpc, $\langle v_{\rm all} \rangle = -256.0 \pm 4.9$ km s^{-1}			
O I λ1302	−321, −214	···	< 13.54
C II λ1334	−321, −214	···	< 13.10
Si II λ1193	−321, −214	···	< 12.54
Si III λ1206	−321, −214	-256.0 ± 4.9	12.48 ± 0.07
Si IV λ1393	−321, −214	···	< 13.04
C IV λ1548	−321, −214	···	< 13.02
MRK335, $\rho = 294$ kpc, $\langle v_{\rm all} \rangle = -240.1 \pm 5.2$ km s^{-1}			
O I λ1302	−275, −180	···	< 13.43
C II λ1334	−275, −180	···	< 12.98
C III λ 977	−275, −180	···	< 12.42
Si II λ1193	−275, −180	−222.4	> 14.09
Si III λ1206	−275, −150	-238.5 ± 5.6	12.41 ± 0.06
Si IV λ1393	−275, −180	-241.1 ± 6.3	12.62 ± 0.09
Si IV λ1402	−275, −150	-247.9 ± 15.5	12.69 ± 0.15
C IV λ1548	−275, −180	-233.7 ± 2.5	13.48 ± 0.04
C IV λ1550	−275, −180	-239.1 ± 5.6	13.40 ± 0.10
O VI λ1031	−278, −150	-215.4 ± 0.9	14.00 ± 0.10

Note. — All the velocities are in the LSR frame. The velocities v_1 and v_2 are the velocities used for the integration of the AOD profiles. A colon means that the estimate is uncertain owing to blending. A "< " sign is a 3σ upper limit, while a "> " sign is lower limit because the absorption reaches the zero-flux level. For the O VI, the errors are dominated by systematics from the correction of the H_2 contamination. $\langle v_{\rm all} \rangle$ is the average velocity between all the ions (observed with COS) where the detection is not blended or uncertain.

3. ABSORPTION STRUCTURE AND ASSOCIATION WITH M31

In the general direction of M31, absorption seen in the spectrum of a QSO can arise from the MW, MW halo (probed by the high-velocity clouds, HVCs, e.g., Wakker 2001), Magellanic Stream (MS), M31 CGM gas, Local Group (LG), or unrelated absorbers at higher redshifts, z. Unrelated absorbers are easily ruled out because for all but one sightline, we use several species and different transitions of the same species to identify the absorption. All the spectra show absorption between about −300 to +50 km s^{-1} for at least one species (all show Si III), separated into different components (see Figs. A1 to A5 in the appendix). The spectra of RXJ0048.3+3941 and HS0033+4300 also show additional absorption between about −450 and −350 km s^{-1} while toward MRK335 two absorption components are observed at −450 and −300 km s^{-1}. We now discuss the origin of these different absorption components based on their velocities.

Milky Way absorption: Saturated absorption is observed in C II, Si II, and Si III between about −70 and +50 km s^{-1} in all the sightlines. The absorption at these velocities arises in the MW disk and halo gas, based on the Galactic disk rotation curve (Clemens 1985).

MW HVC absorption: Lehner & Howk (2011) and Lehner et al. (2012) statistically constrained the distance of the entire HVC population seen in UV absorption using a sample of 28 distant Galactic halo stars and show that no absorption at $|v_{\rm LSR}| \gtrsim -170$ km s^{-1} is observed in the spectra of these stars, implying that any absorption with $v_{\rm LSR} \lesssim -170$ km s^{-1} is beyond 5–15 kpc. This conclusion is further supported by two stars observed with COS through the *HST* programs 12982 and 11592 (PI: Lehner) in the general direction of M31 and M33 (see Fig. 1). These two stars are PG0122+214 ($d = 9.6$ kpc) where HVC absorption is observed at $v_{\rm LSR} \simeq -160$ km s^{-1} (see Lehner et al. 2012) and PG2345+241 ($d = 4.9$ kpc, which is near the MRK335 sightline, see Fig. 1) where HVC absorption is seen at $v_{\rm LSR} \simeq -120$ km s^{-1}. In both cases, the HVC absorption is very weak detected only Si II and C II, not in C IV or Si IV (the Si III cannot be used in stellar spectra owing to the strong damping wings of Lyα). We therefore assign any absorption in the 5 spectra in our sample with $v_{\rm LSR} > -150$ km s^{-1} to the MW and its halo.

MS absorption: Toward the directions of our targets, the MS is not very wide relative to other locations and lies about 12°–22° from our targets. For the Magellanic longitude of our targets, the MS H I emission is observed at $-430 \lesssim v_{\rm LSR} \lesssim -300$ km s^{-1} (Nidever et al. 2008). Absorption velocities is observed in the spectra of RXJ0048.1+3941, HS0033+4300, and MRK335. Since Fox et al. (2014) found a similar distribution in the velocities within 30° of the 21 cm emission from the MS and the H I emission MS velocities throughout the MS body, we will treat the $-430 \lesssim v_{\rm LSR} \lesssim -300$ km s^{-1} interval as potentially arising from the MS. Lockman et al. (2012) also concluded that H I emissions at $v_{\rm LSR} \simeq -400$ km s^{-1} in the general direction of the M31 CGM likely originate from the MS.

M31 absorption: This only leaves the absorption over the range $-320 \lesssim v_{\rm LSR} \lesssim -150$ km s^{-1} identified in red in Figs. A1 to A5 of the appendix, centered at −213 km s^{-1} toward RXJ0048.3+3941, −204 km s^{-1} toward HS0033+4300, −211 km s^{-1} toward HS0058+4213, −256 km s^{-1} 3C66A, and −240 km s^{-1} toward MRK335, which could be either LG or CGM from M31 gas.

The approach used to associate absorbers and galaxies at higher z involves first to estimate 1) the difference between the redshift of the absorber and the systemic redshift of the galaxy ($\delta v = c\,(z_{\rm abs} - z_{\rm gal})/(1 + z_{\rm abs})$) and 2) the impact parameter from the QSO to the galaxy. Then if both conditions, $\rho/R_{\rm vir} \lesssim 1$ and $\delta v \lesssim 200$ km s^{-1}, are

realized, this indicates a physical connection between the absorber and the CGM of the galaxy (e.g., Penton et al. 2002; Wakker & Savage 2009; Prochaska et al. 2011). For example, for the COS-Halos galaxies, a strong clustering of detections was found within $\delta v \leq 200$ km s^{-1} and $\rho/R_{\rm vir} \leq 1$ (Tumlinson et al. 2011). As our selection criterion only targets QSOs at $\rho/R_{\rm vir} \leq 1$, and since the difference between the absorption and the systemic velocity of M31 (-300 km s^{-1} Chemin et al. 2009) is less than 90 km s^{-1}, we associate this gas to the CGM of M31 rather than the LG. The velocities toward the the 5 targets are also within the expected velocities from an extension of a flat rotation curve for M31 (e.g., Chemin et al. 2009). Furthermore these LSR velocities are similar to those observed in H I emission in the CGM of M31 within $\rho \lesssim 150$ kpc (Thilker et al. 2004; Braun & Thilker 2004; Lockman et al. 2012; Wolfe et al. 2013), which all have been connected to the CGM of M31. For all these reasons, we assign the absorption at $-320 \lesssim v_{\rm LSR} \lesssim -150$ km s^{-1} observed in the spectra of our targets to the CGM of M31. We, however, note that absorption at similar velocities is also observed toward several QSOs at larger impact parameters (see Fig. 11 and LG designation in Sembach et al. 2003), but those are all beyond the virial radius of M31. We will analyze this larger sample in a follow-up paper, but we note that with the present sample we find a decrease in the column densities of the ions with increasing ρ (see §§4, and Fig. 2). This relation is not trivial and would not necessarily be expected if this absorption had a different origin. A similar decrease is also observed in the COS-Halos survey (Werk et al. 2013, 2014), strengthening our conclusion that the absorption at $-320 \lesssim v_{\rm LSR} \lesssim -150$ km s^{-1} probes gas from the CGM of M31.

We note that neither in the inner nor in the distant regions do we detect absorption at more negative velocity absorption, as Rao et al. (2013) found in their sightlines near the M31 disk using low resolution COS G140L data. All the detections in the Rao et al. sample are within the disk of M31 and along the major axis (see Fig. 1); they are all consistent with M31 co-rotating disk gas (see Chemin et al. 2009).

4. COVERING FACTOR, KINEMATICS, AND IONIZATION OF THE CGM OF M31

Each sightline shows Si III absorption from the M31 CGM gas, and hence the covering factor is 100% (> 50% at the 95% confidence level for a sample size of 5) for a 3σ sensitivity limit of $\log N_{\rm SiIII} \simeq 11.8$ (assuming FHWM $\simeq$ 40 km s^{-1}). For C IV, 4/5 of the sightlines show absorption down to a sensitivity of $\log N_{\rm CIV} \simeq 12.9$, which corresponds to a covering factor of 80% (> 30% at the 95% confidence level for a sample size of 5). For O VI, we have only two targets probing the inner-most and outer-most regions, and both show O VI absorption associated with the M31 CGM gas. The covering factors for the Si II, C IV, and O VI are all consistent with a high covering factor, but a larger sample will be needed to strengthen this conclusion. For the singly ionized species, the covering factors are only about 100% for $\rho \leq 50$ kpc since there is no detection of C II or Si II beyond 240 kpc.

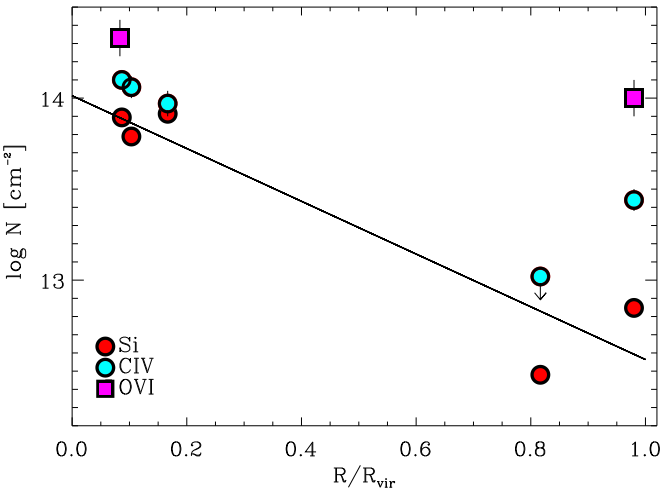

Figure 2. Total column density of Si, C IV, and O VI for the M31 CGM component along each sightline as a function of the impact parameter. At $\rho \leq 50$ kpc, Si is the sum of Si II, Si III, and Si IV; at $\rho = 245$ kpc, Si is Si II (i.e., we assume that the non-detected Si II and Si IV are negligible, see Table 2); at $\rho = 294$ kpc, Si is the sum of Si III and Si IV (i.e., we assume that the non-detected Si II is negligible, see Table 2). The solid line is a linear fit to the Si data points. Data with no visible error bars mean the errors are smaller than the circles.

With 3 sightlines within 50 kpc from M31 and two sightlines at $\rho \geq 245$ kpc, we can also start to assess the variance in the gas properties within the CGM of M31. Below we focus on the differences/similarities in velocities, surface densities, and ionization levels between the inner and distant regions of the CGM of M31.

Within the uncertainties, the absorption observed in the CGM gas at $26 \leq \rho \leq 50$ kpc is at about -210 km s^{-1}, which is $\sim$90 km s^{-1} more positive than the systemic velocity (-300 km s^{-1}) of M31. While there is a large offset from the systemic velocity of M31, the spread in the velocity is not inconsistent with a large co-rotating halo since according to the tilted-ring model of Chemin et al. (2009), where velocities between -300 and -150 km s^{-1} are observed in the disk in the general projected direction of these 3 targets. The two targets (3C66A and MRK335) at $\rho > 240$ kpc have smaller velocity separation from the systemic velocity of M31 of +44 and +64 km s^{-1}.[4] As we noted above the velocities toward the the 5 targets are within the expected velocities from an extension of a flat rotation curve for M31 to about its virial radius (e.g., Chemin et al. 2009).

As for the velocities, at $\rho \leq 50$ kpc, there is no strong evidence for a large variation in the ionization levels or surface densities since the column densities are similar within 1σ for each studied ion (see Table 2). However, between $\rho \leq 50$ kpc and $\rho > 240$ kpc, both the surface densities and ionization levels change drastically. In Fig. 2, we show the total column density of Si (which is the sum of Si II, Si III, and Si IV), C IV, and O VI against ρ, showing a clear decrease in the column densities between $\rho \leq 50$ and > 240 kpc. The column densities are systematically smaller at large ρ, by a factor 10 for Si III

[4] For the MW, a velocity separation of 40–60 km s^{-1} from the systemic velocity would heavily blend this absorption the MW disk component.

and by a factor 5 for Si IV and C IV, but only a factor 2 for O VI. There is no detection of singly ionized species beyond 50 kpc.[5] This implies that the gas is more highly ionized at larger ρ than in the inner region. This can be quantified using the ionic ratios: at $\rho < 50$ kpc, we find $N_{\rm CII}/N_{\rm CIV} \gtrsim 2$–3 and $N_{\rm SiII} \sim N_{\rm SiIII} \sim N_{\rm SiIV}$, while at $240 < \rho < 300$ kpc, we estimate $N_{\rm CII}/N_{\rm CIV} < 0.4$ and $N_{\rm SiII}/N_{\rm SiIV} < 0.6$. We also note that C IV/Si IV~ 5 throughout the CGM of M31 is on the high end of that observed in the MW disk and halo gas (e.g., Lehner et al. 2011; Wakker et al. 2012).

We can directly estimate the fraction of the gas that is ionized by comparing the O I column to the column densities of Si II, Si III, and Si IV (Lehner et al. 2001; Zech et al. 2008). O I is an excellent proxy of H I since they have nearly identical ionization potentials and are strongly coupled through charge exchange reactions (Field & Steigman 1971). O and Si have also the same nucleosynthetic origin (they are both α-elements) and have similar levels of dust depletion in the diffuse gas (Savage & Sembach 1996; Jenkins 2009).[6] Whereas O I arises only in neutral gas, Si II is found in both neutral and ionized gas while Si III and Si IV arise only in ionized gas. Therefore if [O I/Si] $= \log(N_{\rm OI}/N_{\rm Si}) - \log({\rm O/Si})_\odot$ is subsolar, it is because of ionization. Except for HS0033+4300, the S/N of the data allows us to place stringent limits on the column density of O I. Using the results listed in Table 2 we find: [O I/Si] < -1.4 and < -1.1 toward RXJ0048.3+3941 and HS0058+4213 at $\rho \leq 50$ kpc (where Si is the sum of Si II, Si III, and Si IV), [O I/Si II] < -0.1 toward 3C66A at 245 kpc, [O I/Si] < -0.6 toward MRK335 at 294 kpc (where Si is the sum of Si III and Si IV). This implies ionization fractions $\geq 93--97\%$ at $\rho \leq 50$ kpc, and $> 20\%$, $> 75\%$ at 245 and 294 kpc, respectively. It is very likely that the large impact parameter regions are almost entirely ionized too, especially since the mixture of gas-phases favors the more highly ionized phases (see above). However, the overall weaker absorption at $\rho \geq 245$ kpc places a less severe limit on the ionization fraction. The CGM gas of M31 is therefore mostly ionized toward all the targets in our sample. It is also ionized at high levels given the strong absorption of C IV and O VI.

The detections of C IV and O VI at $26 \leq \rho \leq 294$ kpc are particularly important since they provide direct evidence for $\sim 10^5$ K gas and indirect evidence for an extended corona around M31. Indeed for gas with near solar metallicities at 10^5 K, the radiative cooling time is extremely short, implying that the O VI and C IV gas can cool rapidly from a hotter phase (e.g., Gnat & Sternberg 2007), and hence C IV and O VI are often probes of cooling flows or the interface between the cooler gas ($\sim 10^4$ K, Si II, Si III) and the putative hot (10^6 K) corona (e.g., Savage et al. 2003; Lehner et al. 2011; Wakker et al. 2012). The hot corona could provide an alternative explanation for the existence of H I clouds in the CGM of M31 (Spitzer 1956) to that proposed by Wolfe et al. (2013) where they argued that the H I clouds are embedded in an intergalactic filament. However, depending on the exact the physical conditions of the CGM of M31, thermal instability may not be the most viable mechanism for the formation of cooler H I clouds in a disc galaxy as massive as M31 (Binney et al. 2009).

[5] We note, however, that the absorption at more negative velocities assigned with the MS shows detections of C II and Si II at all ρ, again demonstrating the difference between the M31 CGM component and the other velocity components.

[6] we also note that in regions with significant dust, the gas-phase O/Si is expected to be supersolar.

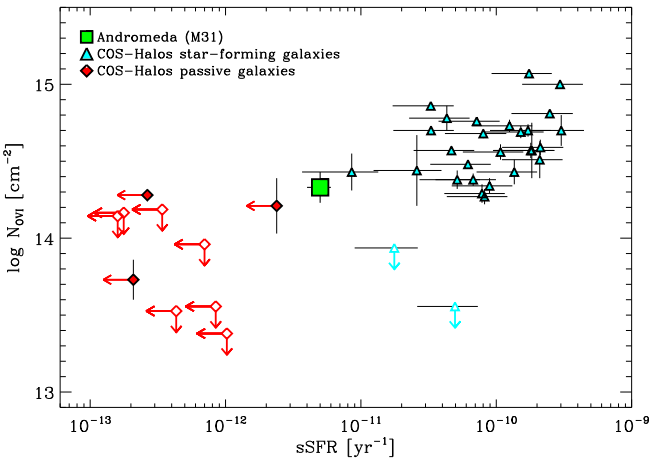

Figure 3. Comparison of the total column density of O VI versus the specific star-formate rate of the galaxy between M31 and the COS-Halos program (Tumlinson et al. 2011). For M31, we only consider the sightline with $\rho = 25$ kpc since the COS-Halos targeted galaxies with $\rho \leq 150$ kpc.

5. METAL AND GAS MASS OF THE CGM OF M31

Having demonstrated the existence of CGM absorption from M31, we now determine the metal and baryon masses of the CGM of M31, a L^* galaxy at $z \sim 0$ and compare it with similar CGM mass estimates from the COS-Halos survey of L^* galaxies at $z \sim 0.5$ (Tumlinson et al. 2011, 2013; Werk et al. 2013, 2014; Peeples et al. 2014). In Fig. 3, we plot $N_{\rm OVI}$ against the specific star-formation rate for M31 and COS-Halos galaxies. M31 is right between the COS-Halos passively-evolving and star-forming galaxies where star-forming systems have typically $\log N_{\rm OVI} \gtrsim 14.3$. The column density of O VI through the M31 CGM is therefore consistent with the transition observed between the COS-Halos passively-evolving and star-forming galaxies, providing additional evidence — independent of that based on its colors — that M31 might be indeed transitioning from a blue to a red galaxy (Mutch et al. 2011; Dalcanton et al. 2012).

The metal mass of the CGM is independent of the metallicity and can be directly determined from the column densities estimated in Table 2. Following Peeples et al. (2014), the mass of metals in the CGM is $M_{\rm Z} = \int 2\pi R \Sigma_{\rm Z}(R) dR$. For Si, $\Sigma_{\rm Si} = \mu_{\rm Si}^{-1} m_{\rm Si} N_{\rm Si}$ is the mass surface density of metals, with $\mu_{\rm Si} = 0.05$ the solar mass fraction of metals in silicon (adopted from Lodders et al. 2009), $m_{\rm Si} = 28 m_{\rm p}$, and $N_{\rm Si} = N_{\rm SiII} + N_{\rm SiIII} + N_{\rm SiIV}$. We use Si here because we have information on its 3 dominant ionization stages in the $T < 10^5$ K ionized gas, requiring no assumption nor a model for the ionization of the cool gas.

We first consider the region $\rho \leq 50$ kpc since we noted in §4 that the column densities for each ion toward the 3 sightlines at $\rho \leq 50$ kpc do not vary much (see Fig. 2).

Using the column densities summarized in Table 2 and averaging the values for Si II, Si III, and Si IV, we find $\langle N_{\rm Si}\rangle = 7.4\times10^{13}$ cm^{-2} at $\rho \le 50$ kpc. We calculate that the mass surface density of metals in the CGM of M31 is

$$\log \frac{\Sigma_{\rm Si}}{\rm M_\odot kpc^{-2}} = 2.6,$$

which is quite similar to the value ($\log\Sigma_{\rm Z} = 3.0$–2.8 at $R = 26$–50 kpc) determined from the empirical fit using the COS-Halos data of L^* galaxies at $z\sim0.5$ (Peeples et al. 2014). Assuming a covering factor of 100% based on the detection of Si III in spectra of the 5 targets in our sample and integrating to 50 kpc, the metal mass of the CGM of M31 is

$$M_{\rm Si} = 2.9\times10^6\ {\rm M_\odot}.$$

If we assume a constant surface density to 150 kpc, then $M_{\rm Si} = 2.6\times10^7\,{\rm M_\odot}$. This is similar to the metal mass estimated for the CGM of COS-Halos L^* galaxies (Peeples et al. 2014). The CGM metal mass within 50 kpc is also comparable to the dust mass in the disk of M31, $M_{\rm d}({\rm disk}) = 5.4\times10^7$ M$_\odot$ (Draine et al. 2014). The corresponding total mass of the CGM of M31 within 50 kpc is then

$$M_{\rm g} = 1429 M_{\rm Si}\Big(\frac{Z_\odot}{Z}\Big) = 4\times10^9\left(\frac{Z_\odot}{Z}\right)\ {\rm M_\odot}.$$

While we do not know the metallicity $Z/Z_\odot$ of the gas, the metallicity of the M31 CGM is unlikely to be much larger than solar. For the CGM of galaxies at $z\lesssim1$, Lehner et al. (2013) found that metallicities range between about $\lesssim0.01$ and $\sim3Z_\odot$, the highest metallicities being associated only with massive outflows (Tripp et al. 2011). In the disk of M31, Sanders et al. (2012) found a scatter between $0.3\lesssim Z/Z_\odot\lesssim4$. The total mass could be much larger if the metallicity is sub-solar. Neither metallicity intervals could decrease the above mass by more than a factor ~3–4. Within $1/6R_{\rm vir}$, the gas mass in the CGM of M31 is therefore comparable to that its disk since $M_g({\rm disk})\approx6\times10^9$ M$_\odot$ using the recent results from Draine et al. (2014). A similar mass of gas was also inferred for the cool CGM of L^* galaxies at $z\sim0.5$ in the COS-Halos survey (Werk et al. 2014).

This mass does not include the hotter highly ionized gas traced by O VI and C IV. If we use C IV (where $\mu_{\rm C} = 0.16$, Lodders et al. 2009) and applying an ionization correction of $f_{\rm CIV} = 0.3$ (which is an upper limit on $f_{\rm CIV}$ in collisionally or photoionized gas, e.g., Gnat & Sternberg 2007; Oppenheimer & Schaye 2013), we find $M_{\rm C} = 2\times10^6(0.3/f_{\rm CIV})(R/50\,{\rm kpc})^2\,{\rm M_\odot}$. This is similar to the mass determined from the O VI COS-Halos survey in the CGM of L^* star-forming galaxy (Tumlinson et al. 2011).

The current sample of sightlines is too small to determine how the mass changes with radius and azimuth since there are only two data points beyond 50 kpc and both of these are at $\rho > 240$ kpc (see Figs. 1 and 2). We noted in §4 a decrease in the column densities with increasing ρ. A linear fit would provide the simplest model for characterizing this observed change in the column density with ρ. In Fig. 2, we show the fit to the data, $N_{\rm Si}(\rho) = 10^{14}\,(\rho/R_{\rm vir})^{-1.45}$ cm^{-2}. This fit is of course poorly constrained, but we note that it is not too dissimilar from the relation determined by Werk et al. (2014, see eqn. 6) for the sample of ∼50 COS-Halos galaxies. Using the result above and integrating to $R_{\rm vir}$, we find $M_{\rm Si}(R_{\rm vir})\sim2$–$3\times10^7$ M$_\odot$ and $M_{\rm g}(R_{\rm vir})\sim3$–$4\times10^{10}$ M$_\odot$. If instead we extrapolate the empirical fit between the surface density and impact parameter, $\log\Sigma_{\rm Si}/({\rm M_\odot kpc^{-2}}) = 3.25-0.0089(R/{\rm kpc})$, determined by Peeples et al. (2014) to 300 kpc, then $M_{\rm Si}(R_{\rm vir})\sim10^8$ M$_\odot$ and $M_{\rm g}(R_{\rm vir})\sim10^{11}$ M$_\odot$. Hence for both methods and even if the covering factor is only 50% (see §3), the CGM mass of M31 is sizable relative to the 10^{11} M$_\odot$ stellar mass of M31 (e.g., Geehan et al. 2006; Tamm et al. 2012).

6. SUMMARY

With *HST*/COS G130M and G160M and *FUSE* archival observations, we study the properties of the gas seen in absorption at LSR velocities $-320\lesssim v_{\rm LSR}\lesssim-150$ km s^{-1} observed in the spectra of 5 sightlines that probe the CGM gas of the M31. Our main results are summarized as follows.

1. Si III is detected toward the 5 targets at $-320\lesssim v_{\rm LSR}\lesssim-150$ km; C IV and Si IV are detected toward 3 targets with $\rho\le50$ kpc and 1 target with $\rho = 294$ kpc; O VI is detected in the two observed sightlines with *FUSE* at $\rho = 26$ and 294 kpc. The covering factors for these ions are therefore consistent with 100% within $R_{\rm vir}$. The singly ionized species are, however, only detected at $\rho\le50$ kpc.

2. Using the O I/Si ionization diagnostic (where Si is the sum of Si II, Si III, Si IV), we demonstrate that the CGM gas of M31 is mostly ($\gtrsim93\%$) ionized. For all the ions, there is evidence for a decrease in the column densities with increasing ρ. The amplitude of this drop is, however, far more pronounced for the singly ionized species than the high ions, implying that the M31 CGM gas is more highly ionized at larger impact parameters.

3. The presence of multiphase gas and absorption of O VI and C IV provide strong evidence for a hot corona within the virial radius of M31.

4. Using Si II, Si III, and Si IV, we estimate a CGM metal mass of 2.9×10^6 M$_\odot$ and a baryonic mass of $4\times10^9\,(Z_\odot/Z)$ M$_\odot$ within $1/6R_{\rm vir}$, implying nearly as much metal and gas mass within $1/6R_{\rm vir}$ of the CGM of M31 as in the disk of M31.

5. A larger sample will be needed to accurately characterize the mass of the CGM as a function of impact parameter and azimuths, but using the empirical model of the surface density for L^* galaxy at $z\sim0.5$ (Peeples et al. 2014) and a linear fit to $N_{\rm Si}(\rho)$, we estimate ~2–10×10^7 and ~3–10×10^{11} M$_\odot$ for the metal and baryonic mass of the CGM gas with $T<10^5$ K at $R_{\rm vir}$. Comparable masses are derived for the highly ionized plasma probed by C IV and O VI.

6. The above conclusions imply that M31 has an extended, massive, multiple gas-phase CGM as observed in higher redshift L^* galaxies. Comparing with the COS-Halos results, we conclude that the CGM of M31 is fairly typical of a L^* disk galaxy that might be transitioning from a blue to red galaxy.

With currently no data at $50 \leq \rho \lesssim 250$ kpc and the projected major and minor axes being poorly populated, it is not possible to accurately determine the behavior of the surface density, and hence the metal and baryon mass distributions, with the impact parameter or the azimuthal angle. It also severely limits the evaluation of cosmological simulations. For example, recent cosmological simulations of 10^{12} $M_\odot$ at $z \sim 0$ by Ford et al. (2014) characterize the properties of the CGM as a function of ρ. They find that the covering factors of the low (e.g., C II) and high (C IV, O VI) ions are all typically high (near 100%) at $\rho < 50$ kpc, but drops much more rapidly at higher impact parameter for the low ions than the high ions. This is broadly consistent with the current observations, but with only 2 data points at $\rho \gtrsim 240$ kpc and no information at $50 \leq \rho \lesssim 250$ kpc, we cannot robustly test the output of these types of simulations. Assessing the output of these simulations would also help us to understand the origins of the metals and baryons in the CGM of M31. Indeed, in these simulations, most of the metal mass comes from recycled accretion at any ρ, but this is very different for the baryons where the total mass at $\rho \lesssim 50$ kpc is largely dominated by recycled accretion (i.e., gas that was once ejected in a wind at least once before), while at $\rho \gtrsim 50$ kpc the ambient gas (i.e., gas is not going to accrete onto a galaxy and that have never been in a wind by $z \sim 0$) dominates the total mass. A large sample of targets that populate the $50 \leq \rho \lesssim 300$ kpc region would make M31 a perfect testbed for theories of galaxy formation and evolution. It would therefore be extremely valuable before the demise of COS to observe many more targets throughout the CGM of M31.

ACKNOWLEDGEMENTS

We thank Jason Tumlinson for sharing the COS-Halos data. NL and JCH acknowledge support for this research provided by National Science Foundation under grant no. AST1212012 and NASA through grants HST-AR-12854 and HST-GO-12982 from the Space Telescope Science Institute, which is operated by the Association of Universities for Research in Astronomy, Incorporated, under NASA contract NAS5-26555. All of the data presented in this paper were obtained from the Mikulski Archive for Space Telescopes (MAST). STScI is operated by the Association of Universities for Research in Astronomy, Inc., under NASA contract NAS5-26555. This research has made use of the NASA's Astrophysics Data System Abstract Service and the SIMBAD database, operated at CDS, Strasbourg, France.

REFERENCES

Barger, K. A., Lehner, N., & Howk, J. C. 2014, ApJ, to be submitted
Besla, G., Kallivayalil, N., Hernquist, L., et al. 2012, MNRAS, 421, 2109
Binney, J., Nipoti, C., & Fraternali, F. 2009, MNRAS, 397, 1804
Braun, R., & Thilker, D. A. 2004, A&A, 417, 421
Brown, T. M., Smith, E., Ferguson, H. C., et al. 2006, ApJ, 652, 323
Brüns, C., Kerp, J., Staveley-Smith, L., et al. 2005, A&A, 432, 45
Chemin, L., Carignan, C., & Foster, T. 2009, ApJ, 705, 1395
Clemens, D. P. 1985, ApJ, 295, 422
Collins, J. A., Shull, J. M., & Giroux, M. L. 2009, ApJ, 705, 962
Dalcanton, J. J., Williams, B. F., Lang, D., et al. 2012, ApJS, 200, 18
Davidge, T. J., McConnachie, A. W., Fardal, M. A., et al. 2012, ApJ, 751, 74
Dekel, A., & Birnboim, Y. 2006, MNRAS, 368, 2
Draine, B. T., Aniano, G., Krause, O., et al. 2014, ApJ, 780, 172
Faucher-Giguère, C.-A., & Kereš, D. 2011, MNRAS, 412, L118
Field, G. B., & Steigman, G. 1971, ApJ, 166, 59
Ford, A. B., Davé, R., Oppenheimer, B. D., et al. 2014, MNRAS[arXiv:1309.5951]
Fox, A. J., Richter, P., Wakker, B. P., et al. 2013, ApJ, 772, 110
Fox, A. J., Savage, B. D., & Wakker, B. P. 2006, ApJS, 165, 229
Fox, A. J., Wakker, B. P., Barger, K. et al. 2014, ApJ, in press [arXiv:1404.5514]
Garrison-Kimmel, S., Boylan-Kolchin, M., Bullock, J. S., & Lee, K. 2014, MNRAS, 438, 2578
Geehan, J. J., Fardal, M. A., Babul, A., & Guhathakurta, P. 2006, MNRAS, 366, 996
Gilbert, K. M., Guhathakurta, P., Beaton, R. L., et al. 2012, ApJ, 760, 76
Gnat, O., & Sternberg, A. 2007, ApJS, 168, 213
Gordon, K. D., Bailin, J., Engelbracht, C. W., et al. 2006, ApJ, 638, L87
Green, J. C., Froning, C. S., Osterman, S., et al. 2012, ApJ, 744, 60
Howk, J. C., Savage, B. D., Sembach, K. R., & Hoopes, C. G. 2002, ApJ, 572, 264
Jenkins, E. B. 2009, ApJ, 700, 1299
Kalberla, P. M. W., Burton, W. B., Hartmann, D., et al. 2005, A&A, 440, 775
Kang, Y., Bianchi, L., & Rey, S. 2009, ApJ, 703, 614
Kereš, D., Katz, N., Weinberg, D. H., & Davé, R. 2005, MNRAS, 363, 2
Lehner, N., & Howk, J. C. 2007, MNRAS, 377, 687
Lehner, N., & Howk, J. C. 2010, ApJ, 709, L138
Lehner, N., & Howk, J. C. 2011, Science, 334, 955
Lehner, N., Howk, J. C., Keenan, F. P., & Smoker, J. V. 2008, ApJ, 678, 219
Lehner, N., Howk, J. C., Thom, C., et al. 2012, MNRAS, 424, 2896
Lehner, N., Howk, J. C., Tripp, T. M., et al. 2013, ApJ, 770, 138
Lehner, N., Keenan, F. P., & Sembach, K. R. 2001, MNRAS, 323, 904
Lehner, N., Staveley-Smith, L., & Howk, J. C. 2009, ApJ, 702, 940
Lehner, N., Zech, W. F., Howk, J. C., & Savage, B. D. 2011, ApJ, 727, 46
Lockman, F. J., Free, N. L., & Shields, J. C. 2012, AJ, 144, 52
Lodders, K., Palme, H., & Gail, H.-P. 2009, Landolt Börnstein, 44
McConnachie, A. W., Irwin, M. J., Ibata, R. A., et al. 2009, Nature, 461, 66
Moos, H. W., Cash, W. C., Cowie, L. L., et al. 2000, ApJ, 538, L1
Morton, D. C. 2003, ApJS, 149, 205
Mutch, S. J., Croton, D. J., & Poole, G. B. 2011, ApJ, 736, 84
Nidever, D. L., Majewski, S. R., & Burton, W. B. 2008, ApJ, 679, 432
Nuza, S. E., Parisi, F., Scannapieco, C., et al. 2014, MNRAS, submitted arXiv:1403.7528
Oppenheimer, B. D., & Schaye, J. 2013, MNRAS, 434, 1043
Peek, J. E. G., Heiles, C., Putman, M. E., & Douglas, K. 2009, ApJ, 692, 827
Peeples, M. S., Werk, J. K., Tumlinson, J., et al. 2014, ApJ, 786, 54
Penton, S. V., Stocke, J. T., & Shull, J. M. 2002, ApJ, 565, 720
Prochaska, J. X., Weiner, B., Chen, H.-W., Mulchaey, J., & Cooksey, K. 2011, ApJ, 740, 91
Putman, M. E., Gibson, B. K., Staveley-Smith, L., et al. 1998, Nature, 394, 752
Putman, M. E., Peek, J. E. G., & Joung, M. R. 2012, ARA&A, 50, 491
Putman, M. E., Peek, J. E. G., Muratov, A., et al. 2009, ApJ, 703, 1486
Ribas, I., Jordi, C., Vilardell, F., et al. 2005, ApJ, 635, L37
Rao, S. M., Sardane, G., Turnshek, D. A., et al. 2013, MNRAS, 432, 866
Richter, P. 2012, ApJ, 750, 165
Ryans, R. S. I., Keenan, F. P., Sembach, K. R., & Davies, R. D. 1997, MNRAS, 289, 83
Sanders, N. E., Caldwell, N., McDowell, J., & Harding, P. 2012, ApJ, 758, 133

Savage, B. D., & Sembach, K. R. 1991, ApJ, 379, 245
Savage, B. D., & Sembach, K. R. 1996, ARA&A, 34, 279
Savage, B. D., Sembach, K. R., Wakker, B. P., et al. 2003, ApJS, 146, 125
Sembach, K. R., Wakker, B. P., Savage, B. D., et al. 2003, ApJS, 146, 165
Shull, J. M., Jones, J. R., Danforth, C. W., & Collins, J. A. 2009, ApJ, 699, 754
Smoker, J. V., Fox, A. J., & Keenan, F. P. 2011, MNRAS, 415, 1105
Spitzer, L., Jr. 1956, ApJ, 124, 20
Stanimirović, S., Dickey, J. M., Krčo, M., & Brooks, A. M. 2002, ApJ, 576, 773
Stocke, J. T., Keeney, B. A., Danforth, C. W., et al. 2013, ApJ, 763, 148
Tamm, A., Tempel, E., Tenjes, P., Tihhonova, O., & Tuvikene, T. 2012, A&A, 546, A4
Thilker, D. A., Braun, R., Walterbos, R. A. M., et al. 2004, ApJ, 601, L39
Thom, C., Peek, J. E. G., Putman, M. E., et al. 2008, ApJ, 684, 364
Thom, C., Putman, M. E., Gibson, B. K., et al. 2006, ApJ, 638, L97
Tripp, T. M., Meiring, J. D., Prochaska, J. X., et al. 2011, Science, 334, 952
Tumlinson, J., Thom, C., Werk, J. K., et al. 2011, Science, 334, 948
Tumlinson, J., Thom, C., Werk, J. K., et al. 2013, ApJ, 777, 59
van der Marel, R. P., Fardal, M., Besla, G., et al. 2012, ApJ, 753, 8
Walterbos, R. A. M., & Kennicutt, R. C., Jr. 1987, A&AS, 69, 311
Wakker, B. P. 2001, ApJS, 136, 463
Wakker, B. P. 2006, ApJS, 163, 282
Wakker, B. P., & Savage, B. D. 2009, ApJS, 182, 378
Wakker, B. P., Savage, B. D., Fox, A. J., Benjamin, R. A., & Shapiro, P. R. 2012, ApJ, 749, 157
Wakker, B. P., Savage, B. D., Sembach, K. R., et al. 2003, ApJS, 146, 1
Wakker, B. P., York, D. G., Howk, J. C., et al. 2007, ApJ, 670, L113
Wakker, B. P., York, D. G., Wilhelm, R., et al. 2008, ApJ, 672, 298
Werk, J. K., Prochaska, J. X., Thom, C., et al. 2013, ApJS, 204, 17
Werk, J. K., Prochaska, J. X., Tumlinson, J., et al. 2014, ApJ, submitted [arXiv:1403.0947]
Wolfe, S. A., Pisano, D. J., Lockman, F. J., McGaugh, S. S., & Shaya, E. J. 2013, Nature, 497, 224
Zech, W. F., Lehner, N., Howk, J. C., Dixon, W. V. D., & Brown, T. M. 2008, ApJ, 679, 460

APPENDIX

Figs. A1 to A5 show the *HST*/COS and *FUSE* absorption-line normalized profiles for the 5 QSO targets in the sample, sorted by increasing impact parameter from the center of M31. The red region in each spectrum shows the M31 CGM component. Absorption at $v_{\rm LSR} > -150$ km s^{-1} is associated with the MW disk and halo. Absorption at $-430 \lesssim v_{\rm LSR} \lesssim -300$ km s^{-1} is associated with the MS.

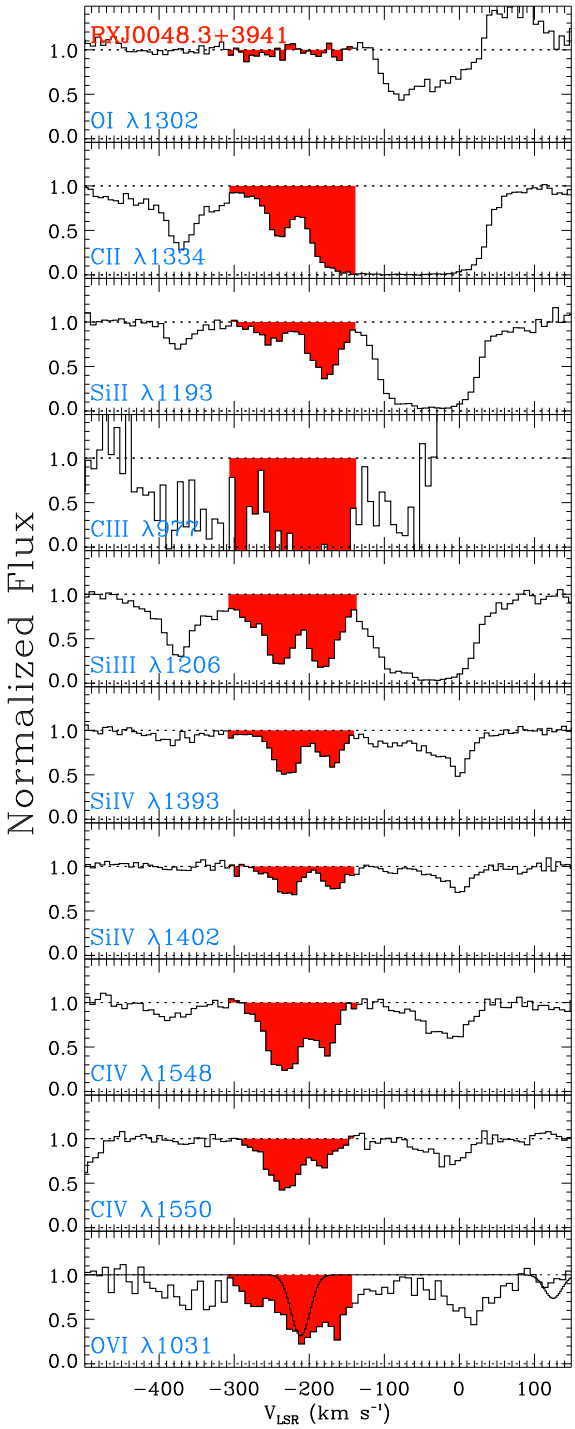

Figure A1. Normalized profiles of RXJ0048.1+3941 at $\rho = 26$ kpc. The spectra were obtained with COS G130M and G160M, except for C III and O VI, which were obtained with *FUSE*. The red region shows the absorption from the M31 CGM gas. The MW and HVC absorption is at $v_{\rm LSR} \gtrsim -170$ km s^{-1}, while the MS absorption is at $-430 \lesssim v_{\rm LSR} \lesssim -310$ km s^{-1}. In the O VI panel, we overplot the H_2 model that was used to correct the O VI absorption from the H_2 contamination. Note that O I is affected by O I airglow emission line at $v_{\rm LSR} \gtrsim -100$ km s^{-1}.

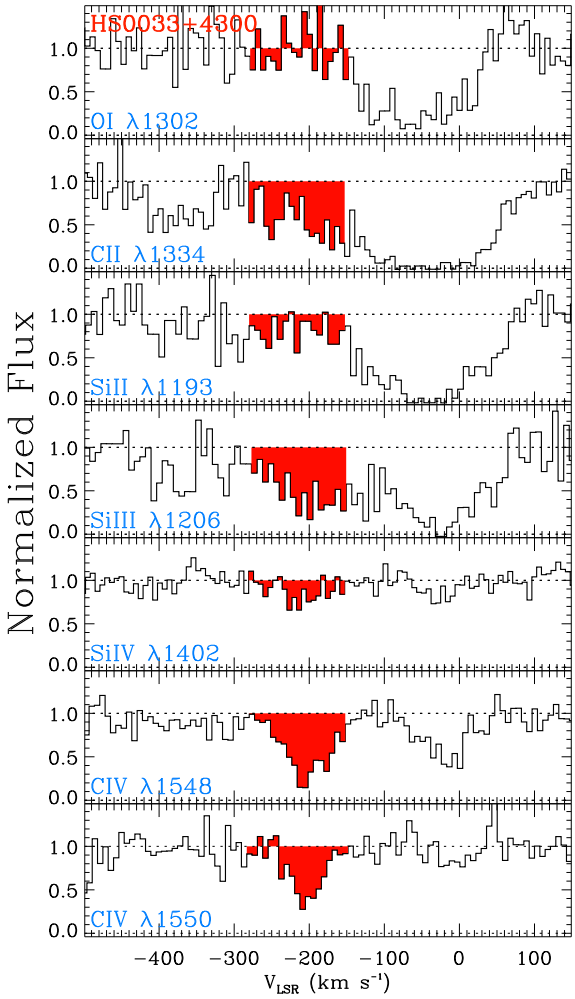

Figure A2. Same as Fig. A1, but for HS0033+4300 at $\rho = 31$ kpc.

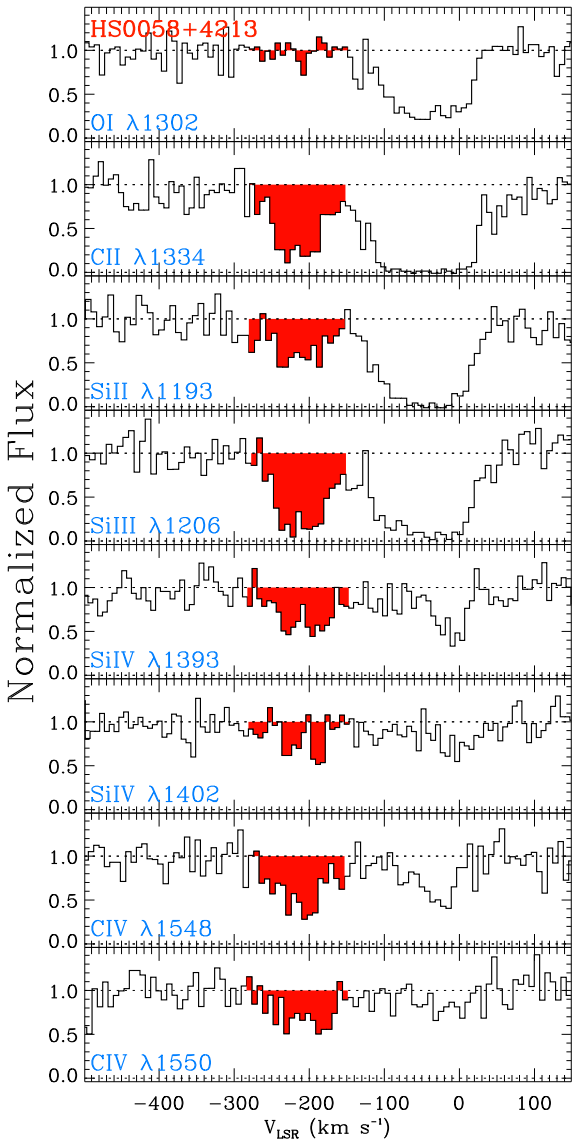

Figure A3. Same as Fig. A1, but for HS0058+4213 at $\rho = 50$ kpc. There is no evidence of MS absortpion toward this sightline.

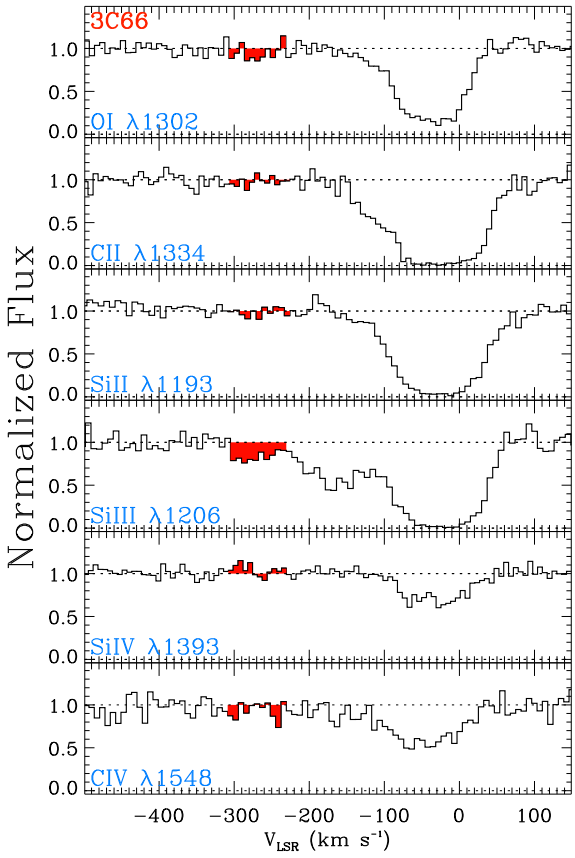

Figure A4. Same as Fig. A1, but for 3C66 at $\rho = 245$ kpc.

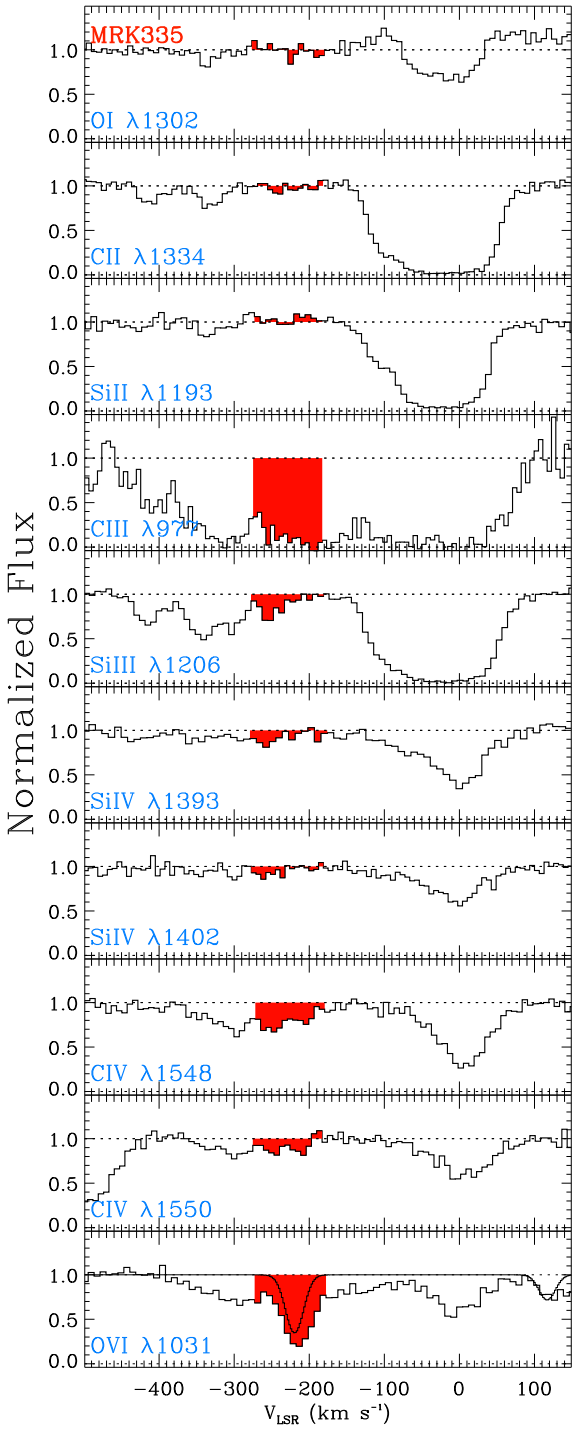

Figure A5. Same as Fig. A1, but for MRK335 at $\rho = 294$ kpc.